Perforation of 12 mm thick steel plates by 20 mm diameter projectiles with flat, hemispherical and conical noses Part II: numerical simulations

T. Børvik[a],*, O.S. Hopperstad[a], T. Berstad[b], M. Langseth[a]

[a] *Structural Impact Laboratory (SIMLab), Department of Structural Engineering, Norwegian University of Science and Technology, N-7491 Trondheim, Norway*
[b] *Livermore Software Technology Corporation (LSTC), Livermore, CA 94550, USA*

Abstract

In Part I of this paper, projectiles with three different nose shapes (blunt, hemispherical and conical) were used in gas gun experiments to penetrate 12 mm thick Weldox 460 E steel plates. It was found that the nose shape of the projectile severely affected both the energy absorption and the failure mode of the target structure during penetration. This part of the paper describes numerical simulations of the problem investigated experimentally. A constitutive model of viscoplasticity and ductile damage for projectile impact has earlier been developed and implemented in the explicit finite element code LS-DYNA. Numerical simulations involving this model have been carried out, and the results are compared with the experimental data. However, numerical problems associated with the element mesh were detected, and adaptive meshing was found necessary in order to obtain reliable results for conical projectiles. From the numerical simulations it is found that the LS-DYNA code is able to describe the different failure modes without any predefined defects in the element mesh if special care is taken, and good agreement is in general obtained between the numerical simulations and experimental results. © 2001 Elsevier Science Ltd. All rights reserved.

Keywords: Penetration; Numerical simulations; Nose shapes; Failure modes; Ballistic limits; Adaptive meshing

1. Introduction

In Part I of this paper [1], projectiles with three different nose shapes (blunt, hemispherical and conical) were used in gas gun experiments to penetrate 12 mm thick Weldox 460 E steel plates.

---

*Corresponding author. Tel.: +47-73-59-46-47; fax: +47-73-59-47-01.
E-mail address: tore.borvik@bygg.ntnu.no (T. Børvik).

Nomenclature

ΔD	projectile nose deformation, i.e. $\Delta D = D_f - D_i$
ΔL	projectile length reduction, i.e. $\Delta L = L_i - L_f$
ΔK	change in kinetic energy
ε	strain
CPU	computational time
d	diameter
D	projectile nose diameter
El	number of removed elements
h	thickness or height
HRC	hardness Rockwell C
K	kinetic energy
L	projectile length
m	mass
T	temperature
t	time
v	velocity
w	deformation
W	work

Subscripts

bl	ballistic limit
c	cavity
ee	eroded elements
f	final value or fracture
g	global part of target
i	initial value
l	local part of target
m	maximum value
p	projectile
pe	permanent value
pl	plug
r	residual value
t	target

From the experimental study it was found that the nose shape of the projectile severely affected both the energy absorption and the failure mode of the target plate during penetration. Hemispherical and conical projectiles penetrated the target mainly by indentation and ductile hole enlargement. In this failure mode most of the material in front of the moving projectile is pushed away laterally. The ballistic limit velocities for these two nose shapes were almost identical and

close to 300 m/s. Blunt projectiles, on the other hand, caused failure by plugging and the ballistic limit velocity was reduced to about 185 m/s. This failure mode is dominated by shear banding. However, at impact velocities above 440 m/s conical projectiles were found to be the most effective penetrator. From a qualitative estimate of the energy dissipation, it was observed that both the local plastic flow around the projectile nose and the global target deformation were most severe for conical projectiles, followed by hemispherical and blunt projectiles in that order. The opposite was observed regarding projectile plastic deformation.

As seen, depending on the specific impact conditions, there may be various modes of failure and energy absorbing mechanisms. Thus, it is utmost important that numerical models used in structural impact problems are able to take these effects into account since the loading situation is never known in advance. A computational model of viscoplasticity and ductile damage for projectile impact has been developed and implemented in LS-DYNA [2] by Børvik et al. [3]. Numerical simulations using this model give results in close agreement with experimental data for plugging failure caused by blunt projectiles [3,4]. The scope of the numerical study presented in this paper is to investigate if the code is able to describe the structural response to projectile impact when different failure modes are expected to occur. This is done by conducting numerical simulations of the experimental tests presented in Part I of the paper. However, it is important to realise that in these highly complex non-linear finite element simulations the material behaviour is not the only matter causing problems. As will be shown, several challenges are associated with the numerical approach itself and special care must be taken in order to avoid errors and premature termination of the analysis. LS-DYNA is a commercial general-purpose finite element code for analysis of large deformation dynamic response of structures based on explicit time integration, and is therefore suitable for the type of problem under investigation. No attempts are made here in order to describe the many different algorithms involved in the numerical simulations. It is referred to the manuals of LS-DYNA [5,2] for more detailed information regarding the numerical scheme, such as the contact–impact algorithm, the automatic mesh generator, the transfer operator and similar.

A limited review on recent papers in the area of numerical modelling of ballistic penetration and perforation was presented by Børvik et al. [4], but surprisingly few papers dealing with such problems have appeared in the open literature. From the literature review, however, it was noticed that adaptive meshing is frequently used in simulations involving penetration. As will be demonstrated in this paper, continuous remeshing provides an alternative to the common practice of elements erosion in Lagrangian codes. In some situations, such as in conical projectile penetration, adaptive meshing was found necessary in order to have reliable results.

2. Constitutive relation

The coupled computational model of viscoplasticity and ductile damage used to predict material behaviour under projectile impact loading has earlier been presented by Børvik et al. [3]. Thus, only the main equations will be given in the following. The model is based on work by Johnson and Cook [6,7], Camacho and Ortiz [8] and Lemaitre [9]. It includes linear thermoelasticity, the von Mises yield criterion, the associated flow rule, isotropic strain hardening, strain rate hardening, softening due to adiabatic heating, softening due to isotropic damage

evolution, and finally a failure criterion. The equivalent von Mises stress σ_{eq} is given as

$$\sigma_{eq} = [1 - D][A + Br^n][1 + \dot{r}^*]^C[1 - T^{*m}], \tag{1}$$

where D is the damage variable; A, B, C, n and m are material constants; r is the damage accumulated plastic strain given as $\dot{r} = (1 - D)\dot{p}$, where p is the accumulated plastic strain [9]; $\dot{r}^* = \dot{r}/\dot{r}_0$ is a dimensionless strain rate, and $\dot{r}_0$ is a reference strain rate; $T^* = (T - T_0)/(T_m - T_0)$ is the homologous temperature, where T is the absolute temperature, T_0 is the room temperature and T_m is the melting temperature of the target material, respectively. The damage variable D takes values between 0 (undamaged) and 1 (fully broken). However, the critical value of damage is found to be <1. Hence, fracture occurs when

$$D = D_C \leqslant 1. \tag{2}$$

A damage evolution rule is proposed as

$$\dot{D} = \begin{cases} 0 & \text{when } p < p_d, \\ \dfrac{D_C}{p_f - p_d}\dot{p} & \text{when } p \geqslant p_d, \end{cases} \tag{3}$$

where D_C is the critical damage, $\dot{p}$ is the plastic strain rate, p_d is the damage threshold and p_f is a fracture strain depending on stress triaxiality, strain rate and temperature given as

$$p_f = [D_1 + D_2 \exp(D_3\sigma^*)]\,[1 + \dot{p}^*]^{D_4}[1 + D_5 T^*]. \tag{4}$$

Here, D_1–D_5 are material constants, $\sigma^* = \sigma_m/\sigma_{eq}$ is the stress triaxiality ratio and σ_m is the mean stress. The first bracket in Eq. (1) describes material degradation due to damage, and the irreversible damage evolution is related to the accumulated plastic strain through Eq. (3). The second bracket in Eq. (1) gives the yield and strain hardening, while the effect of strain rate hardening as proposed by Camacho and Ortiz [8] is expressed in the third bracket. The last bracket in Eq. (1) gives the effect of temperature softening on the equivalent stress. The temperature increase is based on the empirical assumption that 90% of the plastic work under adiabatic conditions is dissipated as heat [10]. Any heat transfer with the surroundings is neglected in this model. When the softening due to damage and temperature exceeds the strain and strain rate hardening, localisation is expected to occur [11]. The model is implemented in LS-DYNA [2] using a fully vectorised backward-Euler integration algorithm [12]. To allow crack growth during penetration, the model is coupled with an element-kill algorithm available in LS-DYNA that removes damaged elements from the mesh when the damage variable reaches the critical value D_C.

   Four different types of tensile tests are required to identify the material constants used in the model [3,13]. Quasi-static tensile tests are used to identify the elastic constants E and v, and the yield stress A of the material. Notched-specimen tensile tests are used to define the strain hardening constants B and n, the critical damage D_C, and the fracture strain constants D_1, D_2 and D_3. Dynamic tensile tests give the viscoplastic constant C and the fracture strain constant D_4. Tensile tests at elevated temperatures provide the constants m and D_5, defining the temperature effect on the stress–strain curve and on the fracture strain, respectively. Thermoelasticity is not included in these simulations (see [4]). For simplicity, the projectile is modelled as a bilinear elastic–plastic strain rate-independent von Mises material with isotropic hardening, and

quasi-static tensile tests were carried out on specimens machined directly from hardened projectiles in order to identify the material constants. All details regarding the model, material tests and calibration procedure can be found in Børvik et al. [3,13]. If not otherwise stated in the text, the model constants listed in Table 1 for the target material of Weldox 460 E steel and in Table 2 for the projectile material of hardened Arne tool steel are used in all simulations.

3. Simulations with a fixed element mesh

Uniform or fixed element meshes are still the most used discretisation method in finite element simulations, and such meshes are known to be both accurate and robust for problems involving small to moderate deformations [14]. However, when large deformations and subsequently large plastic strains are present, meshes become progressively more and more distorted as the deformation increases. Distorted meshes are less accurate and may accordingly introduce numerical difficulties. Thus, in some transient dynamic problems, and in particular those dealing with projectile penetration, uniform element meshes may give severe numerical inaccuracies and eventually an error termination of the simulation.

Here, in the first set of simulations a fixed mesh of 4-node 2D axisymmetric elements with one-point integration and a stiffness based hourglass control was used. Plots of the initial configurations, showing a part of the target plate and the three different projectile nose shapes just prior to impact, are shown in Fig. 1. The target consists of two parts with identical properties in order to study global versus local energy absorption during impact [4]. Recall from the experimental part of the study that the circular target plate has a nominal thickness of 12 mm and a diameter of 500 mm, while the nominal mass and diameter of the hardened projectile were

Table 1
Material constants for Weldox 460 E steel [3]

Elastic constants and density			Yield stress and strain hardening			Strain rate hardening		Damage evolution	
E (GPa)	v	ρ (kg/m^3)	A (MPa)	B (MPa)	n	$\dot{p}_0$, $\dot{r}_0$ (1/s)	C	D_c	p_d
200	0.33	7850	490	807	0.73	5×10^{-4}	0.0114	0.30	0

Adiabatic heating and temperature softening						Fracture strain constants				
C_p (J/kgK)	α	$\bar{\alpha}$ (1/K)	T_m (K)	T_0 (K)	m	D_1	D_2	D_3	D_4	D_5
452	0.9	1.1×10^{-5}	1800	293	0.94	0.0705	1.732	−0.54	−0.015	0

Table 2
Material constants for hardened Arne tool-steel [13]

E (MPa)	v	ρ (kg/m^3)	σ_0 (MPa)	E_t (MPa)	Mean ε_f (%)
204,000	0.33	7850	1900	15,000	2.15

0.197 kg and 20 mm, respectively, in all tests. The exact geometry of the different projectile nose shapes in Fig. 1 is shown in Fig. 2 in Part I of the paper. In each run, the target plate was fully clamped at the support, while the projectile was given an initial velocity similar to the one used in the corresponding experiment. The initial size of the smallest element in the impact region was $0.25 \times 0.2\,\text{mm}^2$ in all simulations, giving a total of 60 elements over the target thickness. In order to reduce the computational time, which is affected both by the element size and number, the mesh was somewhat coarsened towards the boundary. Owing to this coarsening, the total number of elements in the target plate was not more than about 10,000 in the simulations. Contact was modelled using an automatic 2D single surface penalty formulation available in LS-DYNA. In accordance with the experimental observations in Part I of the paper, frictional effects were neglected for blunt projectiles, while a small dynamic frictional coefficient of 0.05 was assumed between all surfaces in contact for conical and hemispherical projectiles.

Earlier simulations have indicated the problem involving shear localisation and plugging for blunt projectiles to be mesh size sensitive [4]. However, the numerical solution using the present model seems to converge monotonically towards a limit solution when the number of elements over the target thickness becomes sufficiently large, i.e. the mesh size dependency is not pathological. It is, therefore, assumed that the numerical results will improve as the element size is reduced, until it stabilises at some value. This is as expected, since the width of a shear band is known to be at the order of 10^1–$10^2\,\mu\text{m}$ [11]. From the metallurgical examination carried out in Part I of the paper (Fig. 8), shear localisation was not found for hemispherical and conical projectiles. Thus, it is assumed that the mesh size sensitivity is most distinct in simulations involving blunt projectiles.

Numerical results from simulations with blunt and hemispherical projectiles are given in Table 3. The computed residual projectile velocities were inserted into the Recht–Ipson [15] model, given in Eq. (1) in Part I of the paper, and the method of least squares was used to estimate the ballistic limit velocities, v_{bl}, and the model constants a and p. These values are given in Table 4 together with the corresponding experimental values. As seen, the agreement with the experimental results is good. While the experimental ballistic limit velocities are 184.5 and 292.1 m/s for blunt and hemispherical projectiles, respectively, the corresponding numerical values are 196.4 and 297.3 m/s, i.e. a non-conservative deviation of 6 and 2%. Also the residual velocity curves, represented by a and p in Table 4, are well predicted by the numerical model. Direct comparisons between numerical and experimental residual velocity curves are shown in Fig. 2. At the highest impact velocities, some more plastic deformation of the projectile takes place experimentally than what is captured in the simulations, especially for hemispherical projectiles. This is partly due to the simplified constitutive model used for the projectile material [4]. Remember also that the experimentally obtained residual velocity curve for the hemispherical projectile was assumed low at the highest impact velocities due to an abnormal projectile deformation in one of the tests (see Part I of the paper). Plots showing perforation of the target plate by a blunt and a hemispherical projectile at impact velocities close to the respective ballistic limits are shown in Fig. 3. Here, fringes of accumulated damage are plotted on the deformed mesh. These plots clearly demonstrated that the numerical model qualitatively captures the overall physical behaviour of the target plate during penetration and perforation.
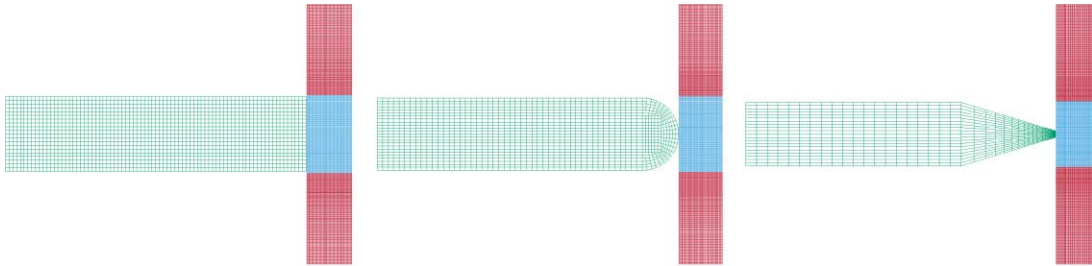
Fig. 1. Plots of the initial configuration showing the different projectiles (green), the local region (blue) and only a part of the global region (red) of the target plate.
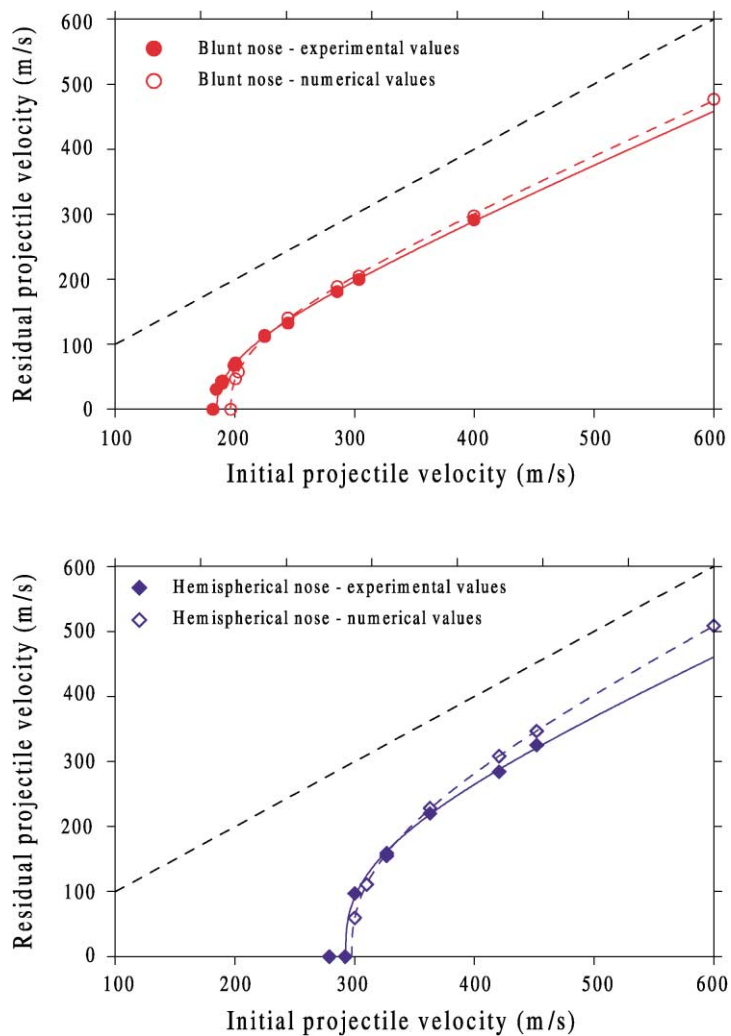

Fig. 2. A comparison between numerical (dotted line) and experimental (solid line) results for blunt and hemispherical projectiles using a uniform element mesh.

Table 3
Numerical results—uniform meshes[a]

v_i (m/s)	v_r (m/s)	v_{rpl} (m/s)	t_f[b] (µs)	El_f (-)	CPU (h)	w_m (mm)	T_m (K)	$K_{fp} + W_p$ (Nm)	$K_{fl} + W_l$ (Nm)	$K_{fg} + W_g$ (Nm)
Blunt projectiles—60 elements over thickness										
600.0	476.8	505	36	257	1.4	0.97	977	22474 + 3115	3063 + 4217	150 + 2441
399.6	297.5	318	40	87	1.3	1.96	869	8747 + 1630	1310 + 2238	142 + 1661
303.5	204.8	242	46	67	1.8	2.43	922	4143 + 905	810 + 1729	155 + 1331
285.4	188.9	230	46	66	1.6	2.41	1072	3528 + 805	705 + 1605	150 + 1230
244.2	140.5	185	56	66	1.7	2.98	844	1954 + 595	465 + 1480	185 + 1195
224.7	111.8	150	68	65	2.0	3.46	1132	1236 + 462	300 + 1514	228 + 1233
202.7	57.6	84	102	63	2.2	5.15	825	329 + 350	105 + 1514	338 + 1495
200.4	47.0	68	117	64	2.9	5.37	810	220 + 330	52 + 1439	375 + 1540
Hemispherical projectiles—60 elements over thickness										
600.0	508.7	545	42	656	4.9	1.42	1453	25481 + 870	1040 + 6163	130 + 1776
452.0	346.9	402	54	672	5.8	2.00	1191	11859 + 300	458 + 5604	193 + 1710
420.6	308.2	375	62	705	3.7[2)]	2.32	1201	9344 + 230	378 + 5551	220 + 1702
362.9	228.3	238	75	697	6.1	3.92	1052	5112 + 154	155 + 5376	265 + 1910
326.7	159.0	210	100	622	8.6	5.89	1036	2461 + 100	130 + 5280	392 + 2150
310.0	110.8	160	124	743	6.9	7.31	1021	1212 + 82	61 + 5179	486 + 2446
300.0	59.6	108	148	947	12.2	9.16	987	355 + 70	15 + 5150	375 + 2900

[a] K_{fp} = final kinetic energy of the projectile; K_{fl} = final kinetic energy of the local part of the target; K_{fg} = final kinetic energy of the global part of the target; W_p = work in the projectile; W_l = work in the local part of the target and W_g = work in the global part of the target.
[b] Complete fracture in the element mesh.

Table 4
Numerical ballistic limits and curves for uniform element meshes

	Blunt			Hemispherical			Conical[a]		
	v_{bl} (m/s)	a	p	v_{bl} (m/s)	a	p	v_{bl} (m/s)	a	p
Numerical	196.4	0.81	2.46	297.3	0.92	2.48	—	—	—
Experimental[b]	184.5	0.79	2.24	292.1	0.81	2.71	290.6	0.95	2.52

[a] Not obtained due to numerical problems.
[b] Experimental results from Part I of the paper [1].

However, numerical problems occurred in simulations with conical projectiles using the fixed element mesh in Fig. 1 and the original material constants from Table 1. Owing to the severe hydrostatic compression of the elements just in front of the nose tip, the actual fracture strain, which is a function of the stress triaxiality ratio, increased dramatically. This delayed the damage evolution process and consequently the erosion of damaged elements. Thus, the elements in the impacted area were significantly distorted, and the time step started to drop. As a final result, the upper nodes in a critical element penetrated the lower nodes, giving a negative element volume
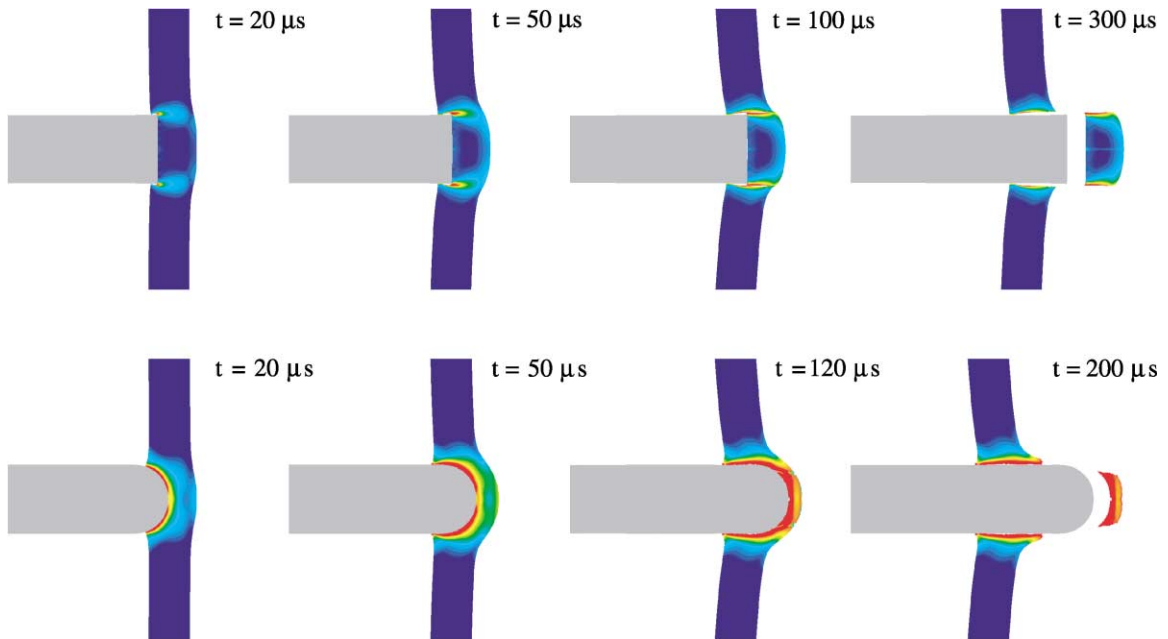
Fig. 3. Perforation of the target plate by blunt (203–60) and hemispherical (300–60) projectiles using a uniform element mesh, plotted as fringes of accumulated damage where red indicates a damage between 0.25 and 0.30 (critical value).
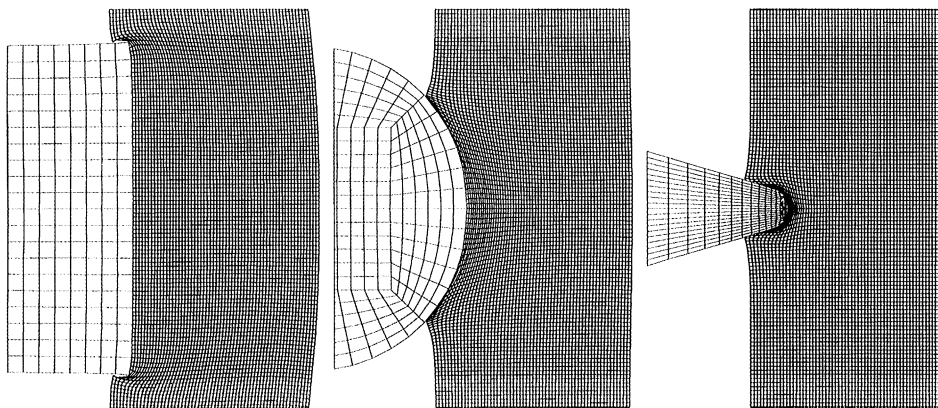

Fig. 4. Element distortions in the target plates just after impact with different projectile nose shapes using a uniform element mesh.

and subsequently an error termination of the simulation. Even though severe distortions were obtained in some elements also with blunt and hemispherical projectiles, error termination occurred only for conical projectiles. The problem is illustrated in Fig. 4, where the element distortion in the target plate just after impact is shown for the three different projectile nose shapes. In an attempt to avoid this problem, two different approaches were explored.

The first approach involved forcing the elements causing problems to erode at an earlier stage. This can easily be done by altering the material constants D_1–D_3 used to describe the strain to failure under different stress states. Fig. 5 shows experimentally measured fracture strains ε_f as a function of the stress triaxiality ratio σ^* [3]. The solid line through the data points is determined from a least square fit of the fracture strain constants D_1–D_3 in the fracture model given by Eq. (4) to the experimental data from quasi-static tensile tests on smooth and notched specimens at room temperature. The strong effect of stress triaxiality on ductility indicated by the model is generally accepted, and has been confirmed experimentally by e.g. Bridgman [16], Hancock and Mackenzie [17] and others. In this study, no experimental data is available for Weldox 460 E under pure shear ($\sigma^* = 0$) and hydrostatic compression ($\sigma^* < 0$), and the extension of the curve into the compression region is solely based on the hydrostatic tension test data. It is thus possible to recalibrate the fracture strain constants to $D_1 = -5.0388$, $D_2 = 6.6198$ and $D_3 = -0.0774$. This gives the almost linear dependence of the fracture strain on the stress triaxiality ratio as shown by the dotted line in Fig. 5. Lindholm and Johnson [18] reported a similar linear trend based on experimental results from the literature. Thus, a reduced fracture strain under hydrostatic compression is obtained, while still having a close fit to the experimental data. Numerical simulations were then carried out with conical projectiles and the new values of the fracture strain constants D_1–D_3. Except for these three values, the numerical model was exactly as before. Plots showing perforation of the target plate by a conical projectile at an impact velocity close to the ballistic limit are shown in Fig. 6, where fringes of accumulated damage are plotted on the deformed mesh. Here, no numerical problems occurred and qualitatively close agreement is found between the simulated behaviour and the experimental results. A negligible plug of 3–4 elements was ejected in some of the simulations. Such plugs were not observed in any of the tests on Weldox 460 E steel, but have been seen in similar experiments on aluminium alloy AA5083.
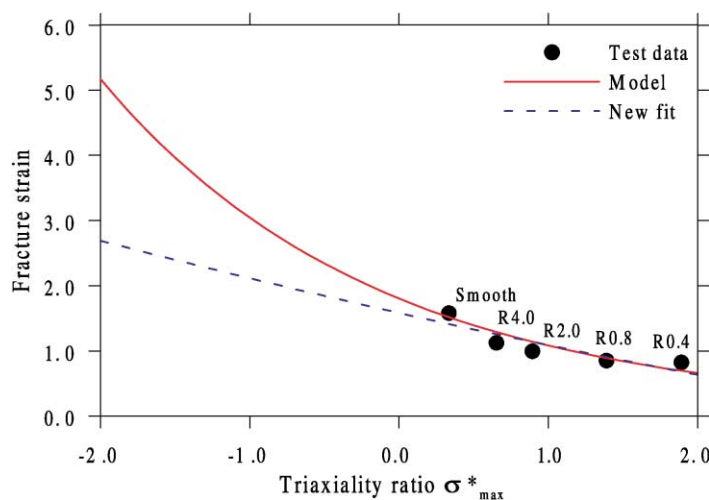

Fig. 5. Fracture strain versus stress triaxiality ratio.

Accurate comparison of results from simulations with different projectile nose shapes requires that all simulations are performed using the same material constants. Therefore, the penetration tests with blunt and hemispherical projectiles were also re-analysed with the new fracture strain constants, and the results are given in Table 5. In a similar way as before, the computed residual projectile velocities were used together with the Recht–Ipson model to estimate the ballistic limit velocities given in Table 6. As seen, the ballistic limits are somewhat reduced due to the reduced fracture strain under hydrostatic compression, while the shape of the residual velocity curves, represented by a and p in Table 6, are less affected by this reduction. If the new ballistic limit velocities are compared to the experimental results also given in Table 6, a conservative deviation of about 8% for all nose shapes are obtained. The residual velocity curves are plotted in Fig. 7. In an exactly similar manner as found experimentally, the ballistic limit velocity for hemispherical and conical projectiles are about equal, while it is considerably lower for blunt projectiles. Also, the residual velocity curves are similar, but one major difference is observed. While the residual velocity curve for hemispherical nosed projectiles merges into the curve for blunt projectiles at high impact velocities in the experiments, the same curve is almost parallel and relatively close to the curve for conical projectiles in the numerical simulations. Except for this discrepancy, the overall agreement between simulations and experimental results is in general good.

As demonstrated above, the main trends in the simulations are similar both when the original and the new fracture strain constants are used, and the effect of reducing the fracture strain appears to be most distinct on the ballistic limit velocity. Thus, it seems safe to compare numerical results and to draw qualitative conclusions based on the simulations with the new fracture strain constants. Fig. 8 compares projectile velocity–time curves and Fig. 9 compares interface force–time curves from simulations just above the respective ballistic limits for blunt, hemispherical and conical projectiles. A similar behaviour as the one measured based on the digital high-speed camera images is obtained (see Fig. 5 in Part I of the paper). This can be used to explain the distinct difference in projectile plastic deformation between the different nose shapes. Even though the impact velocity for the blunt projectile is 50% less than the impact velocity using the conical projectile, the maximum interface force is about 5 times higher and occurs immediately after impact. Cross-sections of the same target plates after perforation are presented in Fig. 10, where fringes of accumulated plastic strain are plotted on the deformed mesh. Here, the fringe colour red indicates a plastic strain above 0.5. While only limited plastic deformations occur outside the localised shear zone for blunt projectiles, the plastic zone is far more extensive for hemispherical and conical projectiles. However, the difference in final cross-section between hemispherical and conical projectiles is small. This difference was much more distinct in the experimental study, as shown in Fig. 7 in Part I of the paper. Maximum target deformations from simulations using the new fracture strain constants are given in Table 5 and shown in Fig. 11. In close agreement with the experimental observations, the deformation is found to decrease from a maximum value at the ballistic limit towards an almost negligible limit value when the impact velocity becomes high. Conical projectiles are also numerically found to give the largest target deformation, followed by hemispherical and blunt projectiles. The maximum deformation is found to be higher numerically than experimentally at identical impact velocities. This is mainly because the numerical values are taken immediately after fracture, while the corresponding experimental values are measured after elastic rebound of the target plate.

Table 5
Numerical results—uniform meshes and new fracture strain constants

v_i (m/s)	v_r (m/s)	v_{rpl} (m/s)	t_f[a] (µs)	El_f (-)	CPU (h)	w_m (mm)	T_m (K)	$K_{fp} + W_p$ (Nm)	$K_{fl} + W_l$ (Nm)	$K_{fg} + W_g$ (Nm)
Blunt projectiles—60 elements over thickness										
600.0	485.1	525	30	563	2.8	1.07	982	23272 + 3291	2489 + 3873	180 + 2355
399.6	302.0	327	38	184	1.8	1.53	758	9012 + 1517	1392 + 2180	129 + 1498
285.4	197.8	219	44	91	1.7	1.96	701	3866 + 767	663 + 1515	131 + 1081
244.2	156.5	191	48	70	1.3	2.08	672	2425 + 561	508 + 1234	136 + 1010
224.7	136.5	171	52	68	1.3	2.18	661	1845 + 473	425 + 1138	142 + 950
200.4	103.5	147	62	64	1.3	2.58	653	1062 + 357	307 + 1110	175 + 945
189.6	85.7	107	72	63	1.4	3.00	636	728 + 295	170 + 1145	209 + 994
179.4	58.3	87	96	63	1.6	3.52	650	355 + 242	113 + 1131	273 + 1056
175.0	35.8	50	126	63	2.1	4.42	654	130 + 229	42 + 1148	271 + 1197
Hemispherical projectiles—60 elements over thickness										
600.0	518.8	565	40	1183	3.2	0.98	1449	26509 + 852	720 + 5988	96 + 1295
452.0	360.6	380	50	853	1.8	1.55	1200	12806 + 300	565 + 5138	130 + 1216
420.6	327.0	365	50	874	2.5	1.83	1146	10529 + 220	302 + 5019	158 + 1224
362.9	248.9	280	72	1303	2.4	2.84	947	6103 + 155	90 + 5106	193 + 1345
310.0	161.5	167	96	1231	2.9	4.79	948	2568 + 110	15 + 4872	335 + 1580
300.0	144.7	200	104	1012	3.8	5.13	1488	2066 + 100	80 + 4651	347 + 1635
292.1	120.0	140	114	1323	6.8	5.99	1003	1425 + 98	20 + 4754	320 + 1800
280.0	78.9	104	130	1492	5.4	7.57	827	617 + 80	10 + 4669	568 + 1790
272.0	36.8	98	140	1100	9.7	8.77	1269	136 + 70	15 + 4520	225 + 2332

v_i (m/s)	v_r (m/s)	v_{rpl} (m/s)	t_f[b] (µs)	El_f (-)	CPU (h)	w_m (mm)	T_m (K)	$K_{fp} + W_p$ (Nm)	$K_{fl} + W_l$ (Nm)	$K_{fg} + W_g$ (Nm)
Conical projectiles—60 elements over thickness										
600.0	539.5	—	26/88	1583	2.9	1.63	847	28382 + 115	2 + 5659	102 + 1200
405.7	311.7	—	36/144	1570	2.1	2.85	772	9475 + 87	2 + 5159	138 + 1351
355.6	242.0	—	42/175	1520	4.9	3.91	733	5713 + 90	2 + 4938	92 + 1620
317.9	172.8	—	48/225	1445	5.6	5.16	821	2916 + 79	2 + 4964	172 + 1821
300.3	136.1	—	50/260	1445	8.3	6.14	819	1809 + 78	2 + 4904	390 + 1700
280.9	80.7	—	56/344	1436	9.1	7.27	854	638 + 67	2 + 4807	405 + 1853
272.0	44.8	—	60/440	1457	9.7	7.65	846	197 + 62	2 + 4781	450 + 1795

[a] Complete fracture in the element mesh.
[b] Time to pierce/time to completely perforate the target.

Table 6
Numerical ballistic limits and curves for uniform element meshes and the new fracture strain constants

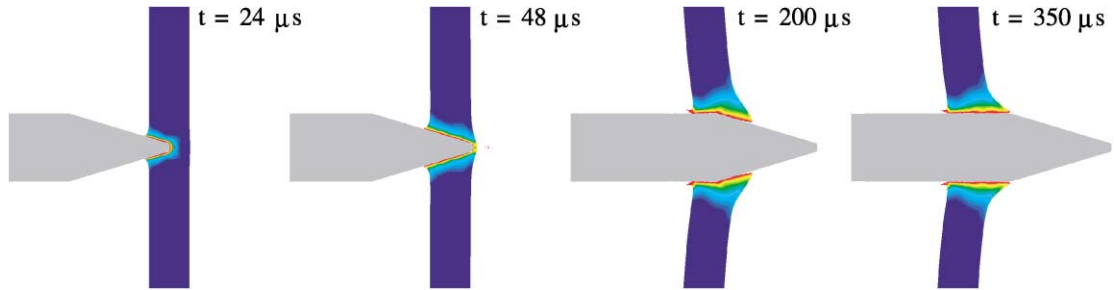|	Blunt			Hemispherical			Conical		
	v_{bl} (m/s)	a	p	v_{bl} (m/s)	a	p	v_{bl} (m/s)	a	p
Numerical	172.0	0.82	2.43	270.6	0.94	2.27	269.0	1.00	2.05
Experimental[a]	184.5	0.79	2.24	292.1	0.81	2.71	290.6	0.95	2.52

[a] Experimental results from Part I of the paper [1].

Fig. 6. Perforation of a target plate by a conical projectile (281–60) using a uniform element mesh and the new fracture strain constants, plotted as fringes of accumulated damage.
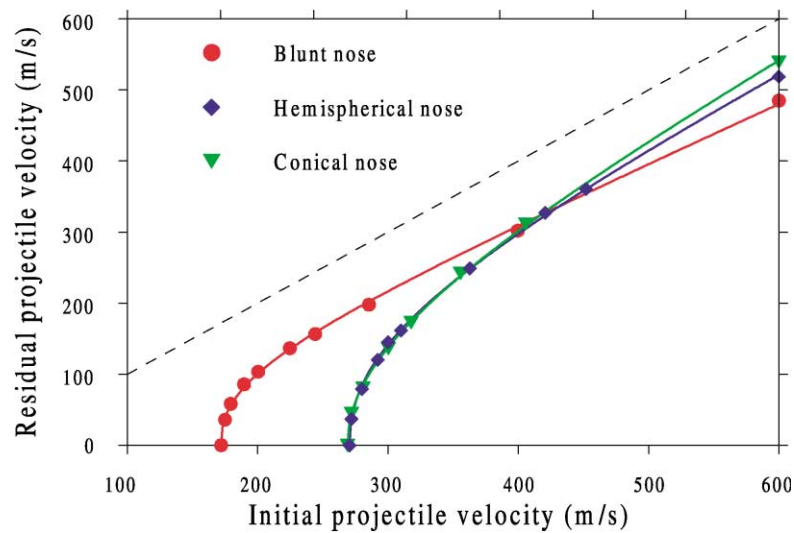

Fig. 7. Residual velocity curves from numerical simulations using a uniform element mesh and the new fracture strain constants.
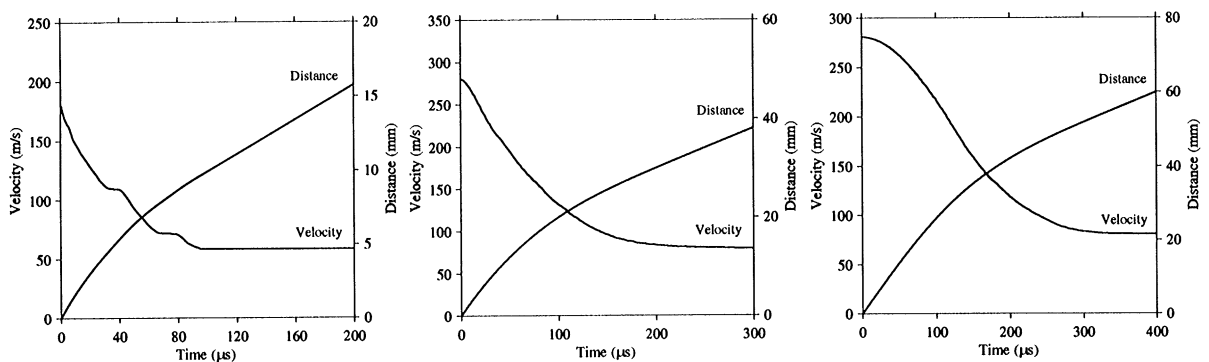

Fig. 8. Velocity–time plots from run (a) blunt 179–60; (b) hemispherical 280–60 and (c) conical 281–60, respectively, in Table 5.
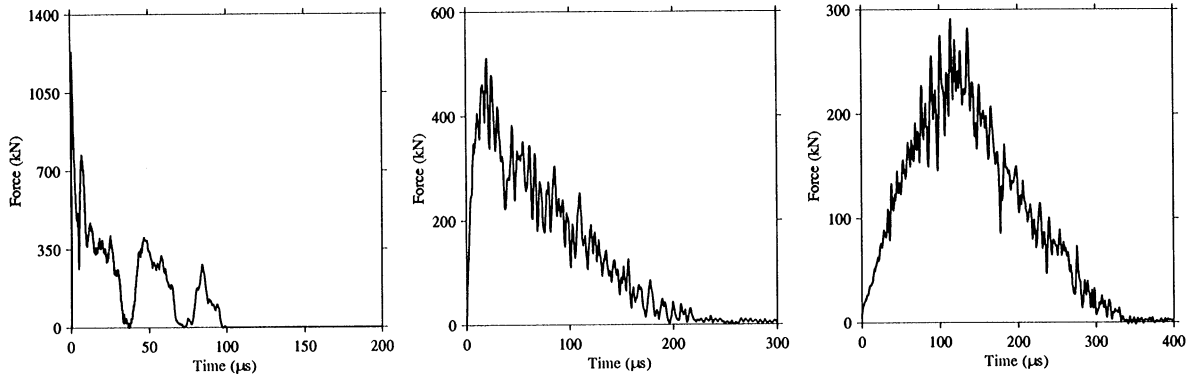
Fig. 9. Force–time plots from run (a) blunt 179–60; (b) hemispherical 280–60 and (c) conical 281–60, respectively, in Table 5.

Fig. 10. Local cross-sections of perforated plates from run (a) blunt 179–60; (b) hemispherical 280–60 and (c) conical 281–60 using uniform element meshes in Table 5 (a red fringe colour indicates a plastic strain above 50%).
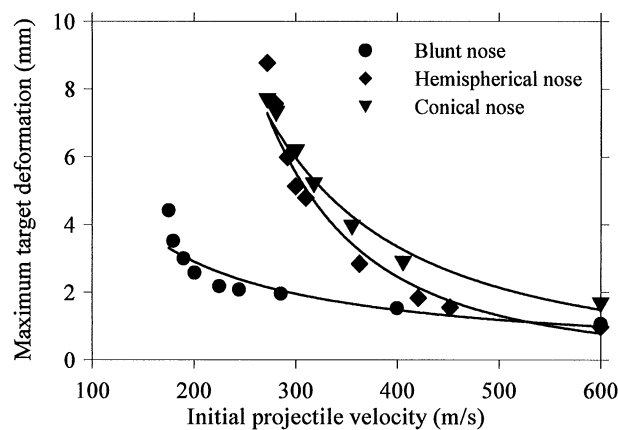
Fig. 11. Maximum target deformation from numerical simulations using a uniform element mesh and the new fracture strain constants.

The amount of energy absorbed during penetration is finally considered. A simple energy balance, given as $\Delta K = W$, indicated at first that some of the initial kinetic energy was lost in the analyses. Small amounts of energy are used in the sliding contact algorithm and in the hourglass control, but this was found negligible in these simulations. However, more severe losses of both energy and mass may take place due to element erosion. This is important in simulations where a

large number of elements are eroded at impact velocities close to the ballistic limit. In the worst case, run 272–60 in Table 5, where a conical projectile and the new fracture strain constants were used, approximately 1500 elements (El_f) were eroded and more than 10% of the total energy was lost. Here, the first number in the identification system refers to the impact velocity, while the second number refers to the total number of elements over the target thickness in the simulation. For most other cases the loss in total energy was much smaller, typically 1–3%. The loss in energy is further illustrated in Fig. 22. In order to take this loss into account, the following procedure was carried out. The target is modelled as one local and one global part with identical properties, as shown in Fig. 1. The border between the parts is placed two element columns, i.e. 0.5 mm, outside the projectile boundary. An examination of the target during perforation shows that all eroded elements are situated within the local part of the plate (see e.g. Fig. 14). Thus, it is reasonable to assume that the total energy loss is due to the loss of internal energy in eroded elements in the local part of the target. In other words, a perfect energy balance is obtained if the total energy loss is added to the local work W_l. This correction has been done both in Tables 3 and 5.

The total amount of initial kinetic energy converted into target and projectile work during impact is given in Table 3 for the original model and in Table 5 for the new fracture strain constants, and the latter is plotted in Fig. 12. As also observed experimentally (see Fig. 10 in Part I of the paper), the amount of work carried out by the system drops from a local maximum at the ballistic limit to a local minimum just after perforation. Then it starts to increase monotonically with impact velocity for blunt and hemispherical projectiles, while the work is almost constant for conical projectiles. Also, numerically blunt projectiles are found to be the most efficient penetrator to a velocity of about 440 m/s. At higher impact velocities, both hemispherical and conical projectiles are more efficient than blunt projectiles. This is in contradiction with the experimental results in Part I of the paper, where hemispherical projectiles were found to be the least efficient penetrator in all tests.
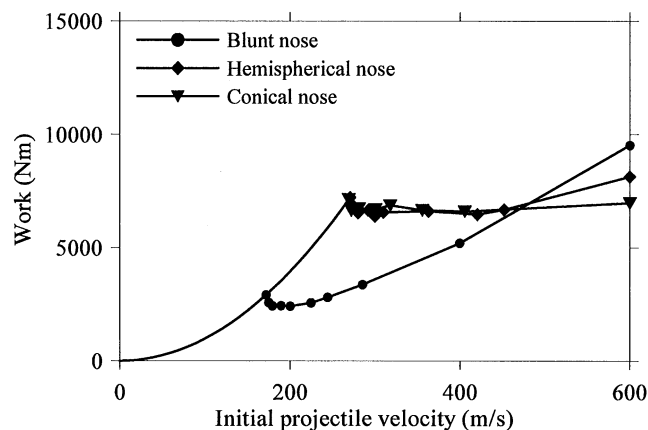

Fig. 12. Change in projectile kinetic energy ($\Delta K = W$) given as a function of initial projectile velocity using a uniform element mesh and the new fracture strain constants.

Details from the energy calculations are plotted in Fig. 13 for simulations using the new fracture strain constants. As seen, the energy absorption for hemispherical and conical projectiles is very similar, while blunt projectiles show a somewhat different behaviour. First, the amount of energy absorbed by the blunt projectile itself is considerable and increases with impact velocity, while the local work is moderate due to the localised plugging failure. Second, the amount of global target work increases with velocity for blunt projectiles. For hemispherical and conical projectiles, the global work decreases with impact velocity within the stated velocity range, and the local target work is very high. These results may have been affected by the chosen location of the border between the local and global parts in the model.

As also illustrated in Fig. 14, many elements are eroded in simulations with hemispherical and conical projectiles. Severe erosion of elements also appears for blunt projectiles at the highest impact velocities, but in these simulations the effect is of minor importance in the energy balance. Moreover, the lower the fracture strain becomes the more elements are eroded. Consequently, hemispherical and conical projectiles erode the material in front of the nose instead of pushing it out laterally as seen experimentally, and neither conservation of mass nor energy is achieved. In coming versions of LS-DYNA, it is possible to store both the energy and mass of eroded elements in the history variable to satisfy the conservation laws.

Even though fixed element meshes give good results, particularly in plugging failure close to the ballistic limit, there is a need for a more physically correct method for conical projectiles since the approach of adjusting the fracture strain constants obtained in material tests is unacceptable. Thus, the second approach used in this study is adaptive meshing without altering the material constants in the constitutive model.
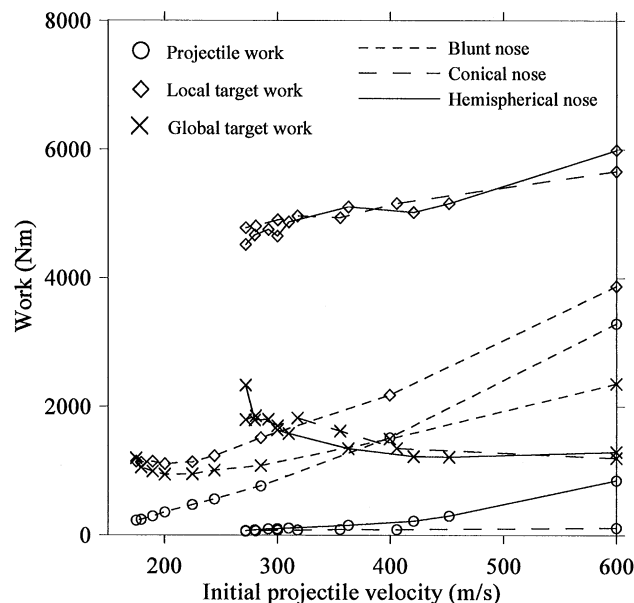

Fig. 13. Energy absorbed in global and local deformation during penetration using a uniform element mesh and the new fracture strain constants.
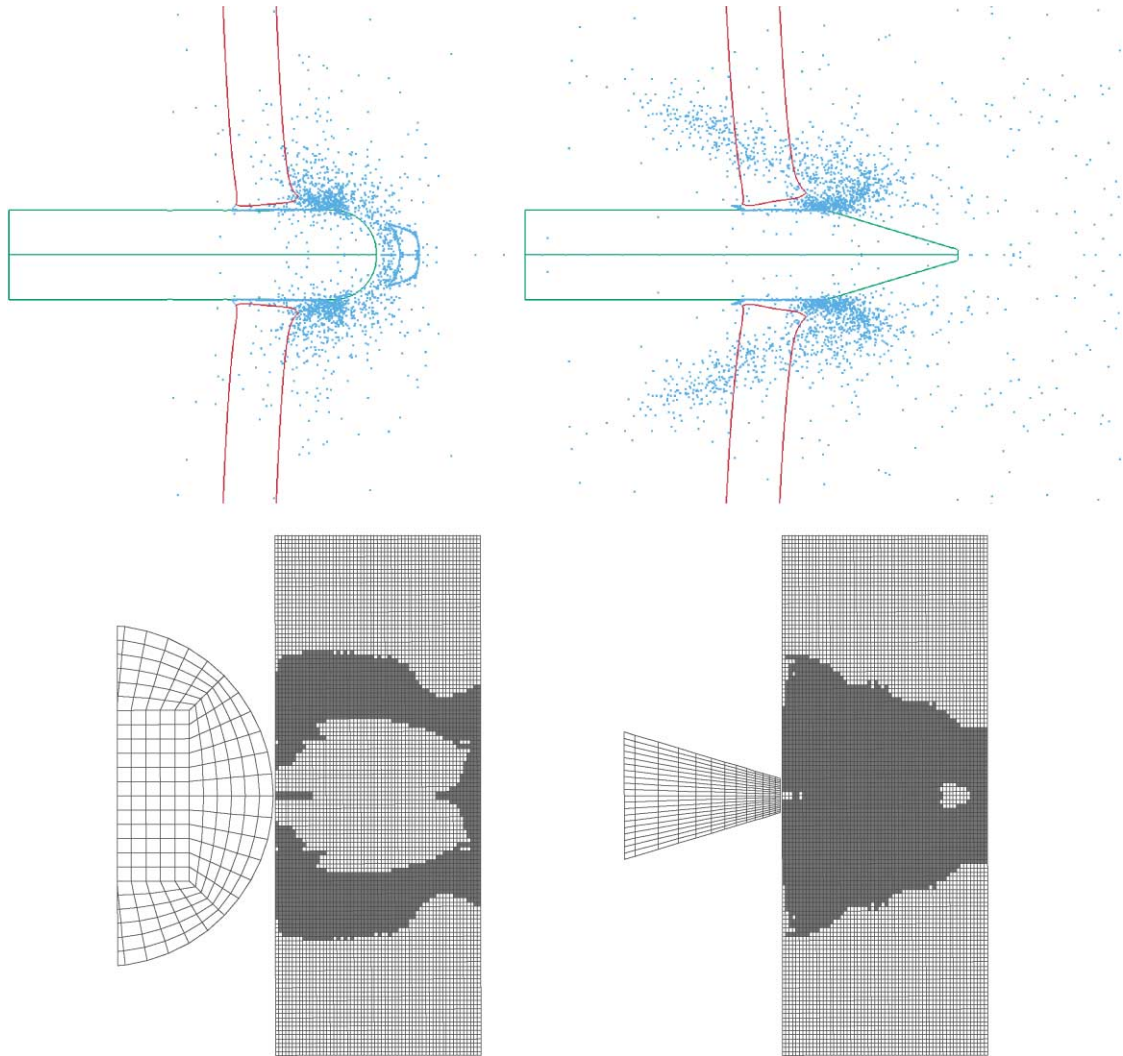
Fig. 14. Plots showing deleted nodes (as the black area) in simulations using hemispherical (300–60) and conical (281–60) projectiles, respectively, and the new failure strain constants.

4. Simulations with adaptive meshing

As seen, Lagrangian solution techniques based on a fixed element mesh generally works well as long as the element distortion is moderate. But, in the presence of large deformations such as in ballistic penetration, finite elements may become severely distorted (see Fig. 4). This in turn may cause premature termination of the analysis, or give unacceptably small time steps. Therefore, in some situations an Eulerian approach that is not affected by deformation-induced mesh distortions may seem necessary. However, as pointed out by Camacho and Ortiz [8], Eulerian formulations of ballistic penetration suffer from several shortcomings. This has enforced the development of alternative methods to avoid numerical problems due to mesh disturbances. The

simplest approach is to use an erosion or element kill technique as in the previous chapter, where troublesome elements simply are removed from the mesh in accordance with a failure criterion. However, this technique is as just demonstrated not always adequate (see Fig. 14). Other techniques, such as the coupled ALE (Arbitrary–Lagrangian–Eulerian) formulation or the more resent "meshless methods" [19], have been developed to solve problems involving large plastic flow in localised areas. The latter method also seems to have a great potential in describing propagating discontinuities, such as arbitrary crack growth in brittle materials.

However, the approach that has received most attention during the last decade is probably the adaptive meshing technique. This method is used to extend the domain of application in Lagrangian codes. Adaptive meshing is generally classified into several groups. In the present version of LS-DYNA [2] only two of these are available. The first method is often referred to as *r*-adaptivity, moving grid adaptivity or rezoning. Here, the number of elements and nodes are tried fixed, while the nodal positions are relocated to achieve optimal aspect ratios of the elements within a part at predefined time intervals. The second available method, called fission *h*-adaptivity, subdivides the elements into smaller elements whenever an error indicator shows that subdivision of these elements is necessary for improved accuracy. Unfortunately, the fission process can only be applied to specific groups of shell elements, and *r*- and *h*-adaptivity cannot be combined in the present version of LS-DYNA.

The advantages of using adaptive meshing in ballistic penetration are undoubtedly many [8]. It enables the simulation of large plastic flow in a Lagrangian framework. It may also include the possibility to obtain a solution of comparable accuracy using much fewer elements, and hence less computational resources than with a fixed mesh. Rezoning ensures good element aspect ratio, thus preventing severe mesh distortions and unacceptable small time steps in the simulations. The major disadvantage with the method is the possible introduction of inaccuracies and smoothening of the results during mapping of the history variables. In this study, 2D *r*-adaptivity is used in combination with a simplified approach to imitate the advantages of *h*-adaptivity in the penetration problem. Since the simulations with blunt and hemispherical projectiles worked satisfactory using a fixed element mesh, rezoning was only crucial for the conical projectiles. However, in order to be able to compare the results, all tests were re-analysed using adaptive meshing.

The adaptive method available in the commercial version of LS-DYNA was originally intended for forging operations, and not for ballistic penetration involving failure. Thus, in order to carry out simulations some new features had to be implemented in the code. First, it was not possible to rezone only the local part of the target plate, while keeping the global part fixed. This resulted in a complete relocation of the entire element mesh at each rezoning, also in the relatively inactive parts at the boundary, causing an increase in both computer time and data storage requirements. To solve this problem, a subroutine that refines the element mesh from the boundary towards the centre by a predefined factor was implemented. This could be done since the zone of large deformation gradients, giving severe mesh distortions, always is at the centre of the target in these particular tests. Thus, the method imitates the advantage of *h*-adaptivity, which keeps the order of the elements unchanged while seeking to improve the solution by adaptive mesh refinement and coarsening in active and inactive areas, respectively. In this study, a scale factor of 10 was used in the radial direction in all simulations, which means that there are 10 times more elements over the thickness in the impacted region than at the boundary. One disadvantage with this approach is

that only a single part can be modelled, so that there is no longer possible to study local versus global energy absorption in the target during penetration. Secondly, there was a need to modify the algorithm in LS-DYNA used to detect a new contour when propagating cracks due to eroded elements formed new parts such as a plug or fragments. The automatic mesh generator used this new contour to construct a completely new mesh within the part. Since the mesh generator required uniquely defined closed contours in order to work, it was necessary to automatically divide the original part into two or several closed parts to avoid an error termination at failure in the element mesh. Nodal values for all variables to be remapped are generated using a least square best fit. A completely new mesh is then generated from the old mesh at each remeshing interval. In the new mesh, the elements are adjusted towards a given characteristic element size. Finally, the remeshed regions are initialised by interpolation of stresses, displacements and velocities from nodal point values in the old mesh to the corresponding new nodal positions.

In fact, only one additional parameter (and some default values) is needed in the input file in order to run adaptive simulations. This parameter, ADPFREQ, defines the time interval between adaptive refinements. For blunt projectiles, ADPFREQ was adjusted to give approximately 10 adaptive refinements in each run. For hemispherical and conical projectiles, many more refinements were required, and as many as 100 were used in some of the simulations. As pointed out by Scheffler and Zukas [20], such frequent rezoning may render the computational mesh semi-Eulerian and give the results a smoothness characteristic of Eulerian calculations. A second input is also demanded, ADPTOL, but this is just the characteristic element size, equal to the smallest element in the impact region. However, the algorithm used to detect the new contour, which again was used by the automatic mesh generator in LS-DYNA to generate a new mesh, was rather unstable and caused error if the lines defining the contour overlaid each other or if internal eroded elements were present at rezoning. The instability problems increased with number of elements, and it was for that reason decided to run all adaptive simulations with a characteristic element size of $0.3 \times 0.375 \, \text{mm}^2$, giving only 40 elements over the target thickness. The potential effect of mesh size sensitivity in adaptive simulations will not be discussed in this paper. Except for these parameters, the numerical model with the adaptive mesh was exactly the same as the model with the fixed mesh, using the original material constants as given in Tables 1 and 2.

Numerical results from adaptive simulations are given in Table 7, while ballistic limit velocities and curves, estimated from the Recht–Ipson model, are given in Table 8. Since the results from adaptive simulations are not as easily available as in fixed mesh simulations the content in Table 7 is somewhat reduced compared to Tables 3 and 5. The excellent aspect ratio of the elements just in front of the projectile after rezoning is clearly seen in Fig. 15. These plots should be compared with Fig. 4 where the fixed element meshes are shown just after impact. Notice also from Fig. 15 how the element mesh shapes and forms around the nose of the projectile as it slides into the target. No numerical problems appeared when using conical projectiles and the original fracture strain values when rezoning was allowed. Fig. 16 shows some detailed plots from the perforation process using different projectile nose shapes and adaptive meshing. Also, qualitatively good agreement is obtained between simulations and experiments. Note that the remeshing continues after complete fracture. This is important, especially for conical projectiles, since the perforation process continues even though the target has been pierced. The final cross-section of a target plate perforated by a conical projectile at an impact velocity close to the ballistic limit is shown in Fig. 17. As seen, the cross-section is more similar to the experimental cross-section (see Fig. 7 in

Table 7
Numerical results—adaptive meshing

v_i (m/s)	v_r (m/s)	v_{rpl} (m/s)	t_f (μs)	El_f (-)	CPU (h)	w_m (mm)
Blunt projectiles—40 elements over thickness						
600.0	476.1	512	36	94	0.6	0.62
399.6	295.1	321	41	42	1.1	1.92
303.5	199.6	234	48	44	1.3	2.09
285.4	179.3	218	53	41	1.6	2.46
244.2	126.6	171	66	46	2.6	3.85
224.7[a]	114.3	157	65	65	8.7	3.66
224.7	98.9	121	78	39	3.3	3.70
210.0	54.0	83	105	41	4.6	5.21

v_i (m/s)	v_r (m/s)	v_{rpl} (m/s)	$t_f{}^b$ (μs)	El_f (-)	CPU (h)	w_m (mm)
Hemispherical projectiles—40 elements over thickness						
600.0	506.7	553	42	157	7.6	0.63
452.0	344.9	400	57	244	1.1	1.59
362.9	228.6	249	81	163	1.6	2.90
326.7	161.5	215	90	117	2.0	5.04
310.0	114.5	146	110	104	2.5	6.20
300.0	54.3	98	150	126	3.1	9.24
Conical projectiles—40 elements over thickness						
600.0	523.0	—	26	157	1.3	0.50
405.7	304.0	—	36	90	1.6	3.21
355.6	228.9	—	40	99	2.1	4.29
317.9	161.3	—	44	69	1.8	5.36
300.3	120.6	—	48	59	2.0	6.68
280.9	46.1	—	61	51	3.1	8.89

[a] This simulation was carried out using 60 elements over the target thickness.
[b] Complete fracture in the element mesh.

Table 8
Numerical ballistic limits and curves for adaptive meshing.

	Blunt			Hemispherical			Conical		
	v_{bl} (m/s)	a	p	v_{bl} (m/s)	a	p	v_{bl} (m/s)	a	p
Numerical	203.8	0.82	2.37	297.8	0.92	2.48	278.3	0.96	2.19
Experimental[a]	184.5	0.79	2.24	292.1	0.81	2.71	290.6	0.95	2.52

[a] Experimental results from Part I of the paper [1].

Part I of the paper) than the corresponding cross-section shown in Fig. 10 using a fixed mesh. Thus, when rezoning is allowed the material in front of the projectile nose is pushed out laterally instead of being eroded. This is also clearly seen from the number of eroded elements (El_f) in the
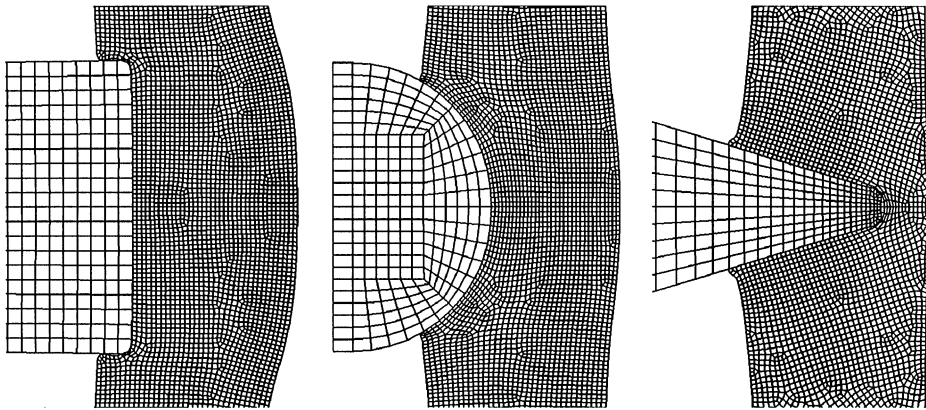
Fig. 15. Details of element meshes just after remeshing in adaptive simulations.

simulations given in Tables 3, 5 and 7. While approximately 1500 elements were eroded in the simulation using a fixed element mesh and the new fracture strain constants, only about 60 elements were eroded in the corresponding simulation using rezoning. Vector plots of the nodal displacements can be used to study the material flow in the target after impact. The direction of the flow is found very similar to the one obtained microscopically, i.e. a lateral flow of the material in front of the projectile. This was not the case using a fixed element mesh, where the material flow essentially was parallel to the direction of the moving projectile. Finally, Fig. 18 illustrates the coarsening of the element mesh towards the boundary during perforation of the target by a conical projectile. As seen, the mesh is much denser around the projectile nose where the rate of deformation is most intense. Notice also that in these plots, only a part of the complete target plate is shown.

Residual velocity curves are plotted in Fig. 19 for simulations where rezoning is used. It is interesting to observe that both the ballistic limit velocity and the parameters a and p defining the residual velocity curve (see Table 8) for blunt and hemispherical projectiles using adaptive meshing are close to the corresponding values using a fixed element mesh and the original material constants (see Table 4 and Fig. 7). This gives confidence to the adaptive method used in the simulations. In contrast to both the experimental results and the numerical results using a fixed element mesh and the new fracture strain constants, there is a small difference between the ballistic limit velocities for hemispherical and conical projectiles. However, this difference is not more than 7% and the shapes of the residual velocity curves are close. If compared to the experimental results, the deviation in ballistic limit velocities using adaptive meshing and the original fracture strain constants is 10%, 2% and 4% for blunt, hemispherical and conical projectiles, respectively. The increased deviation in ballistic limit for blunt projectiles may be due to the coarser element mesh used in the adaptive calculations than in the fixed mesh simulations. A direct comparison between experimental and numerical results using rezoning for the conical projectiles is shown in Fig. 20. Finally, Fig. 21 shows that the perforation times obtained from the different numerical simulations are similar and close to the experimental values estimated from the high-speed camera images (see Part I of the paper). The perforation times are slightly lower using a fixed
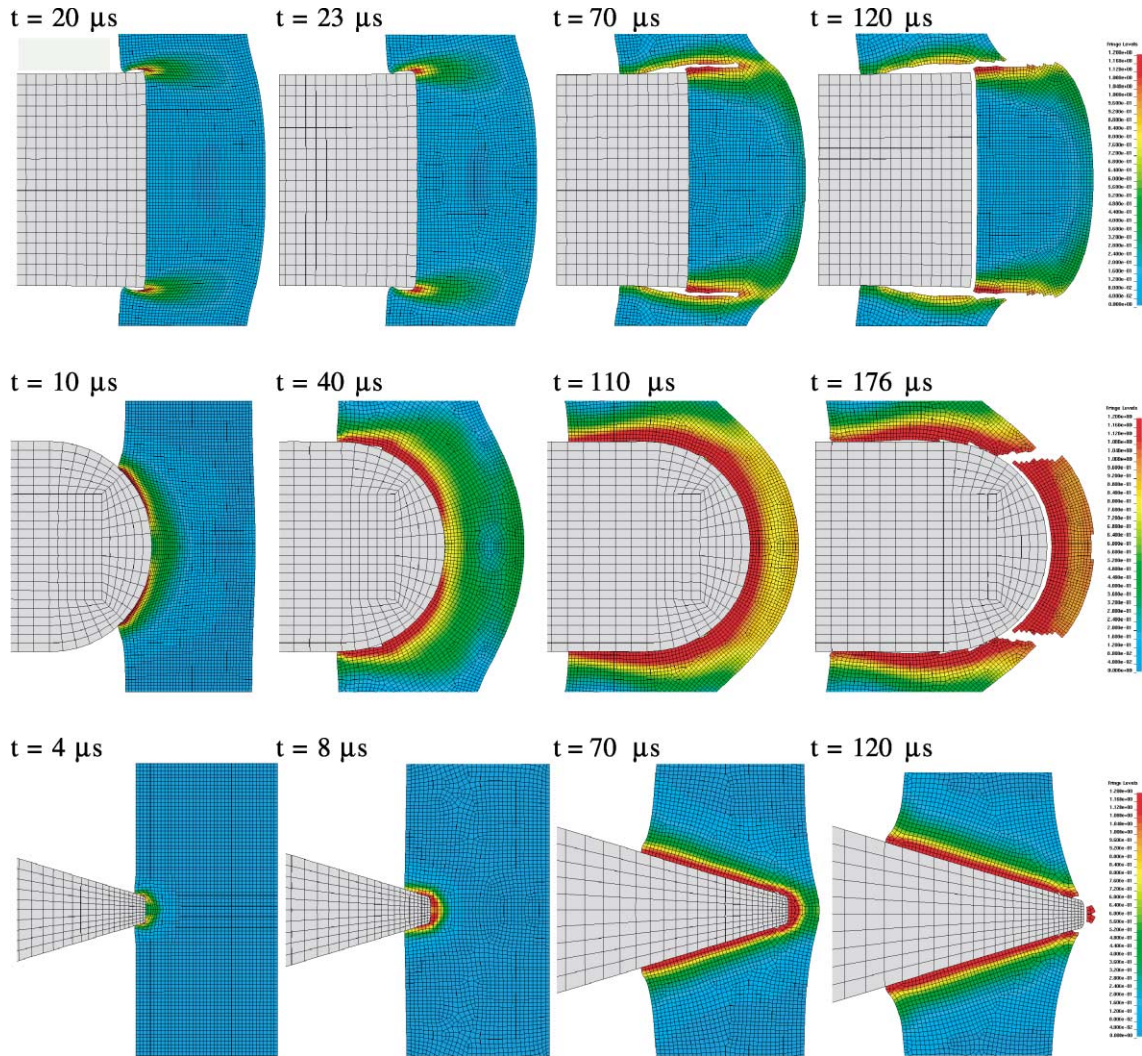
Fig. 16. Close-ups of blunt (225–40), hemispherical (300–40) and conical (300–40) projectiles perforating the target plate using adaptive meshing (see Table 7 for details). Fringes of accumulated plastic strain in the user defined range $p = 0$ (blue) to $p = 1.2$ (red) are shown.

Fig. 17. Final cross-section of target plate perforated by conical projectile (from run 300–40 in Table 7) using adaptive meshing and plotted with fringes of accumulated plastic strain (a red fringe colour is equal to a plastic strain above 50%).
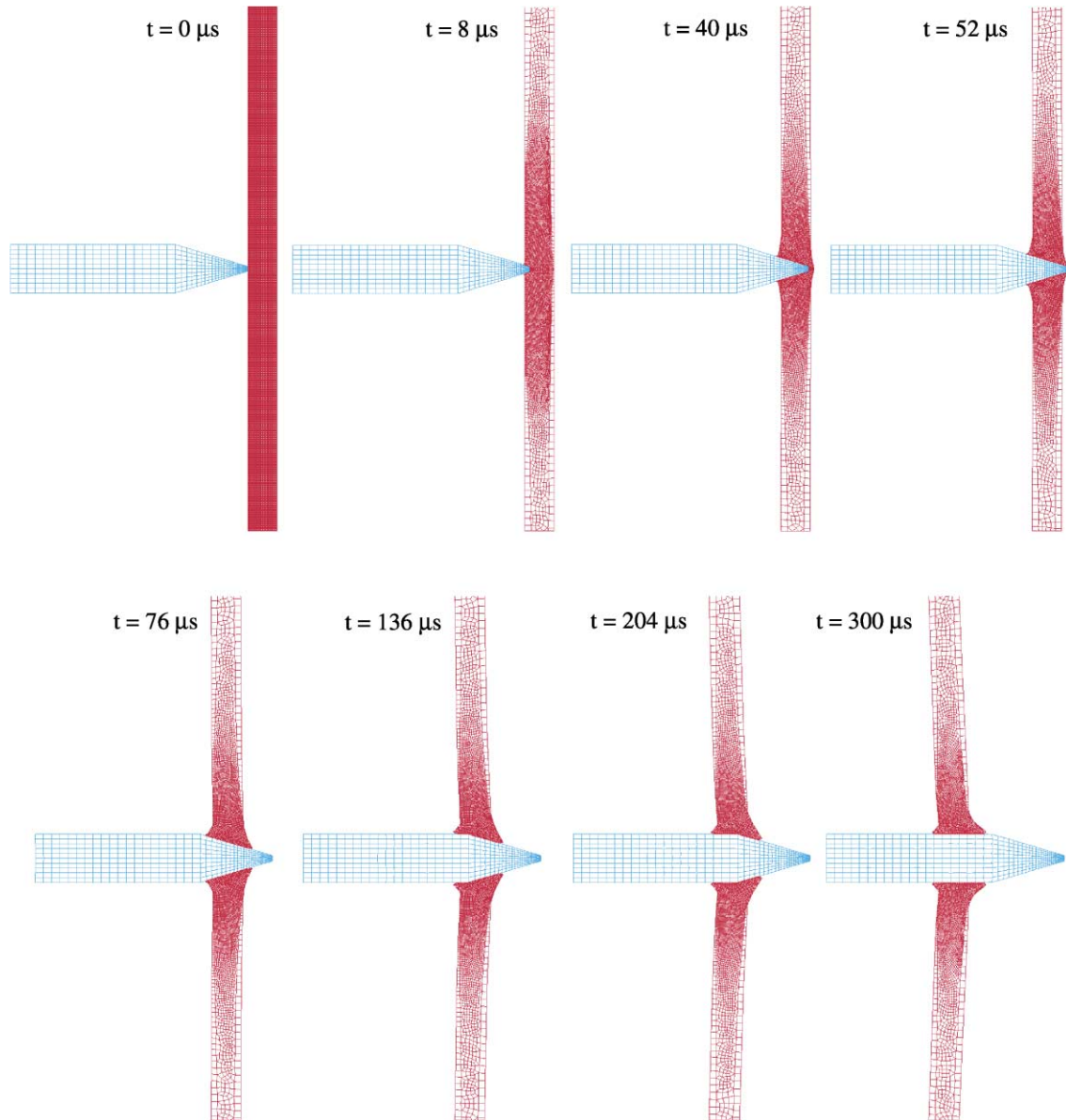
Fig. 18. Outline of the target plate perforated by a conical projectile (from run 300–40 in Table 7) using adaptive meshing.

mesh and the new fracture strain constants than for the other models at identical impact velocities.

Since there is only one part in the target plate using adaptive meshing, it is not possible to study local versus global energy absorption during penetration. The energy ratios, defined as $\Delta K/W$, from some of the simulations are shown in Fig. 22. This figure shows that the energy ratios for blunt projectiles (Fig. 22a) are close to unity, independent of numerical method, which again
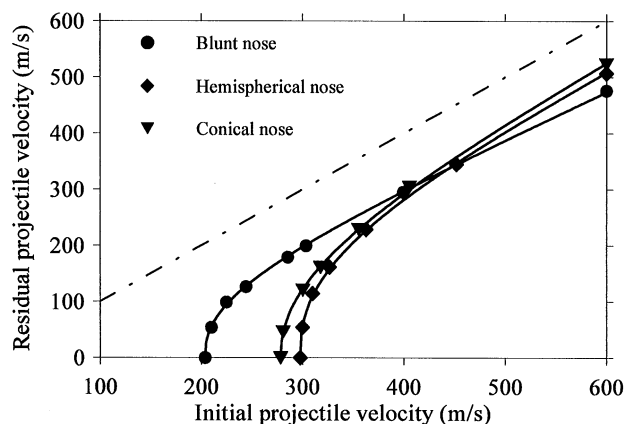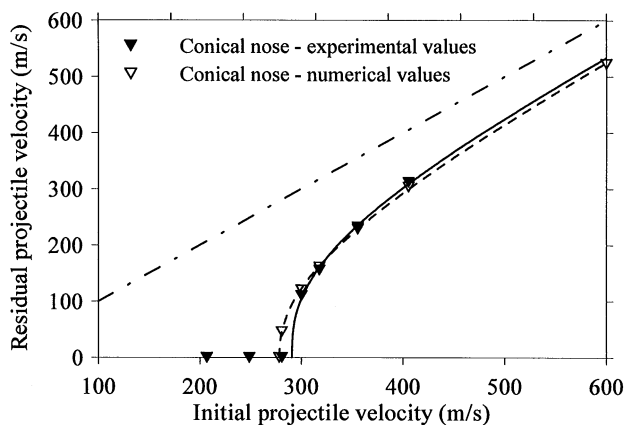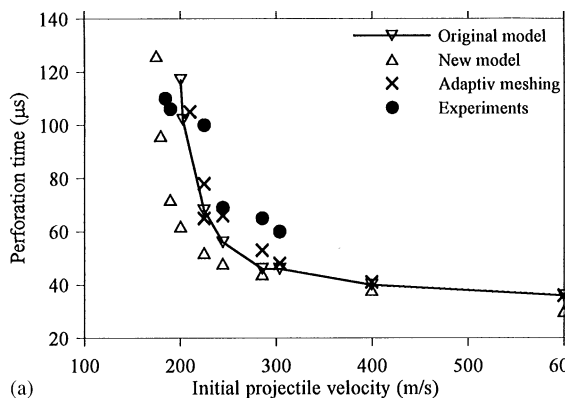
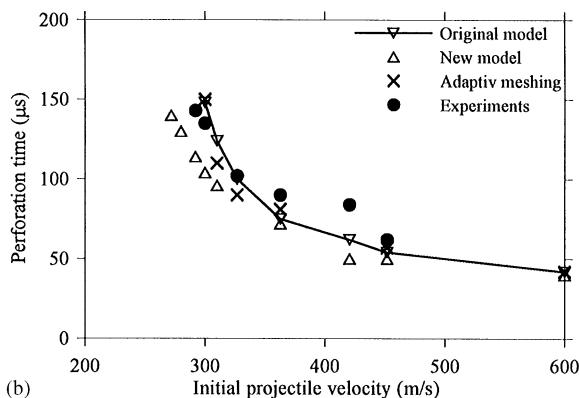Fig. 19. Residual velocity curves using adaptive meshing.

Fig. 20. A comparison between numerical (dotted line) and experimental (solid line) results for conical projectiles using adaptive meshing.

Fig. 21. Comparison between perforation times versus impact velocities for (a) blunt and (b) hemispherical projectiles.
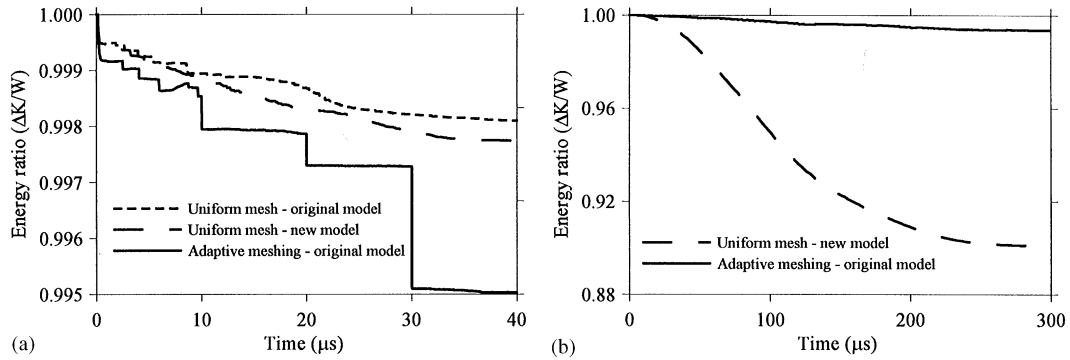
Fig. 22. Energy ratio in simulations using (a) blunt projectiles ($v_i = 600\,\text{m/s}$) and (b) conical projectiles ($v_i = 300\,\text{m/s}$).
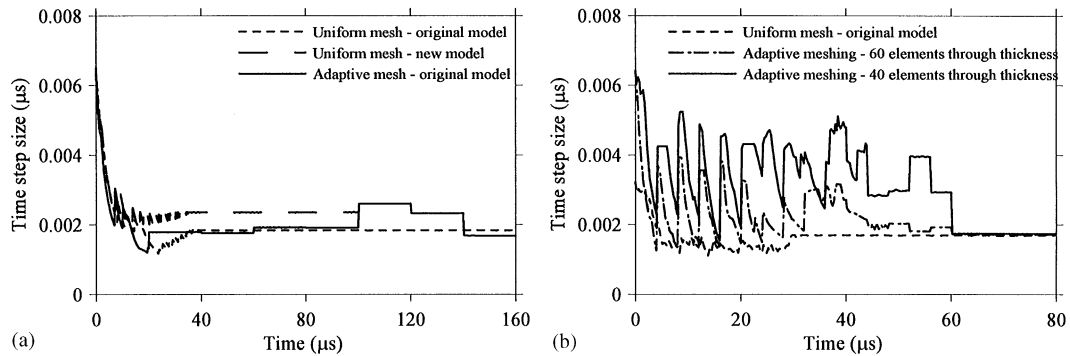

Fig. 23. Comparison between time steps using uniform meshes versus adaptive meshing for (a) blunt projectiles ($v_i = 225\,\text{m/s}$) and (b) conical projectiles ($v_i = 356\,\text{m/s}$).

shows that there are hardly any energy losses in the simulations even at the highest impact velocities where the number of eroded elements may be considerable. For conical projectiles, on the other hand, much more energy is lost using a fixed mesh. As shown in Fig. 22b, nearly 10% of the energy is lost in a simulation close to the ballistic limit. According to Scheffler and Zukas [20], energy losses greater than 10% in the sliding interface prescription are usually indicative of a serious problem. Almost no energy is lost in the corresponding simulation using adaptive meshing. Thus, conservation of energy is also fulfilled for conical projectiles when rezoning is introduced. A comparison of time step size histories for the different numerical cases is shown in Fig. 23 for blunt and conical projectiles. In order to have a reliable evaluation, the two adaptive simulations were re-calculated using 60 elements over the target thickness. Thus, the initial element size was identical in these simulations. Since there is no refinement and coarsening of the element mesh in the adaptive strategy, the expected superior performance was to some extent absent. The time step size is seen to be almost equal for blunt projectiles, independently of numerical strategy. This indicates that the distortion of the smallest elements in plugging failure is similar in adaptive and fixed mesh calculations. Using conical projectiles, the situation is

somewhat different. Here, the elements in front of the nose tip are severely deformed, and the time step size is reduced accordingly using a fixed element mesh. By way of contrast, the aspect ratio is optimised in the rezoning procedure using adaptive simulations. This is illustrated in Fig. 23b, where a distinct increase in the time step size is seen when critical elements are rezoned. Nevertheless, it is seen from the required CPU-times listed in Tables 3, 5 and 7 that the differences in computational time is not considerable, and usually between 1 and 10 CPU-hours on the HP workstations used in this study.

5. Concluding remarks and summary

The use of computer codes to solve transient dynamic problems is today commonplace, and a large number of commercial FE codes exist. These codes are applied to problems ranging from fairly low to extremely high damage levels [20]. Thus, it becomes increasingly important to validate that code predictions correspond to the real physical behaviour of impacted structures, especially if different failure modes are expected to appear. In this paper, more than 60 different numerical simulations are reported, running several hundred CPU-hours on either a HP C360 or a HP J5000 workstation. The numerical results are compared with 24 different high-precision, large-scale impact tests (see Part I of the paper). In other words, both the numerical and experimental evidences are considerable, and this gives somewhat more confidence to the reported observations.

In general, close correlation between numerical and experimental results is achieved. Important parameters in the penetration problem such as ballistic limit velocity, residual projectile velocity, shape of residual velocity curve, maximum target deformation, perforation time and energy absorption, are all well predicted using numerical simulations. Hence, the computational methodology presented in this paper seems to work well for ductile targets perforated by deformable projectiles with different nose shapes in the sub-ordinance velocity regime. The model is formulated within a Lagrangian framework, which has many advantages in ballistic penetration. It is furthermore shown that rezoning plays an important role in order to avoid critical element distortions and severe numerical problems, such as those reported for conical projectiles. Thus, adaptive meshing enlarges the field of application for the Lagrangian formulation and is undoubtedly an attractive alternative to the common practice of element erosion. Some main conclusions from the simulations are given below:

- Both the ballistic limit velocity and the residual velocity curve were in close agreement with the experimental results for blunt and hemispherical projectiles using a fixed element mesh and the original computational material model proposed by Børvik et al. [3]. If compared to the experimental results, a non-conservative deviation in ballistic limit velocity of 6 and 2% for blunt and hemispherical projectiles, respectively, were obtained.
- Numerical problems occurred when perforation by conical projectiles were tried simulated using a fixed element mesh and the original material constants. This was due to severe hydrostatic compression in front of the projectile nose tip that delayed the element erosion process and finally caused an error termination of the simulation.

- In the first attempt of avoiding this problem, the material constants describing the fracture strain under hydrostatic compression was reduced, causing troublesome elements to erode at an earlier stage. This made it possible to simulate perforation of the target plate also by conical projectiles. Qualitatively, good correlation with the experimental results was obtained. However, a closer examination revealed that the elements in front of the nose tip of both hemispherical and conical projectiles were mainly eroded instead of being pushed away laterally as observed experimentally. This caused, among other factors, unacceptable large energy losses in the simulations.

- Adaptive meshing was finally applied. After some changes in the rezoning capability available in LS-DYNA, good agreement was obtained. Both the ballistic limit velocity and the residual velocity curve were almost identical for blunt and hemispherical projectile using either a fixed mesh or adaptive meshing. No numerical problems occurred with conical projectiles and the original fracture strain constants when rezoning was allowed, and the energy loss due to eroded elements was small. If compared to the experimental results, the deviation in ballistic limit velocity using adaptive meshing is 10%, 2% and 4% for blunt, hemispherical and conical projectiles, respectively.

- At the highest impact velocities, plastic deformation of the projectile may become severe and this absorbs a lot of the initial kinetic energy. The simple material model used in these simulations for the projectile is not able to describe this behaviour correctly. Thus, the coupled computational model of viscoplasticity and ductile damage used for the target plate should in following simulations also be calibrated for the projectile material.

Acknowledgements

References

[1] Børvik T, Langseth M, Hopperstad OS, Malo KA. Perforation of 12 mm thick steel plates by 20 mm diameter projectiles with flat, hemispherical and conical noses. Part I: experimental study. Int J Impact Eng 2002;27:19–35.

[2] LSTC. LS-DYNA user manual, Version 950, Livermore Software Technology Corporation, CA, USA, 1999.

[3] Børvik T, Langseth M, Hopperstad OS, Malo KA. Ballistic penetration of steel plates. Int J Impact Eng 1999;22(9–10):855–87.

[4] Børvik T, Hopperstad OS, Berstad T, Langseth M. Numerical simulation of plugging failure in ballistic penetration. Int J Solids Struct 2001;38(34–35):6241–64.

[5] LSTC. LS-DYNA theoretical manual, Livermore Software Technology Corporation, CA, USA, 1998.

[6] Johnson GR, Cook WH. A constitutive model and data for metals subjected to large strains, high strain rates and high temperatures. In: Proceedings of the Seventh International Symposium on Ballistics, The Hague, 1983.

[7] Johnson GR, Cook WH. Fracture characteristics of three metals subjected to various strains, strain rates, temperatures and pressures. Eng Fract Mech 1985;21(1):31–48.

[8] Camacho GT, Ortiz M. Adaptive Lagrangian modelling of ballistic penetration of metallic targets. Comput Meth Appl Mech Eng 1997;142:269–301.

[9] Lemaitre J. A course on damage mechanics,, 2nd ed.. Berlin: Springer, 1996.

[10] Bammann DJ, Chiesa ML, Horstemeyer MF, Weingarten LI. Failure in ductile materials using finite element simulations. In: Jones N, Wierzbicki T, editors. Structural crashworthiness and failure. Amsterdam: Elsevier, 1990. p. 1–54.

[11] Bai Y, Dodd B. Adiabatic shear localization: occurrence, theories and applications. Oxford: Pergamon Press, 1992.

[12] Berstad T, Hopperstad OS, Langseth M. Elasto-viscoplastic constitutive models in the explicit finite element Code LS-DYNA3D. In: Proceedings of the Second International LS-DYNA3D Conference, San Francisco, USA, September 20–21, 1994.

[13] Børvik T, Hopperstad OS, Berstad T, Langseth M. Computational model of viscoplasticity and ductile damage for projectile impact. Eur J Mech A/Solids 2001, in press.

[14] Belytschko T. On difficulty level in non linear finite element analysis of solids. Bull Int Assoc Comput Mech 1996;2:6–8.

[15] Recht RF, Ipson TW. Ballistic perforation dynamics. Int J Appl Mech 1963;30:384–90.

[16] Bridgman PW. Studies in large plastic flow and fracture. New York: McGraw–Hill, 1952.

[17] Hancock JW, Mackenzie AC. On the mechanisms of ductile failure in high-strength steels subjected to multi-axial stress-states. J Mech Phys Solids 1976;24:147–69.

[18] Lindholm US, Johnson GR. Strain rate effects in metals at large shear strains. In: Proceedings of the 29th Sagamore Army Materials Conference entitled Material Behaviour under High Stress and Ultrahigh Loading Rates, New York, 1982.

[19] Belytschko T, Krongauz Y, Organ D, Fleming M, Krysl P. Meshless methods: an overview and recent developments. Comput Meth Appl Mech Eng (Special issue on Meshless Methods) 1996;139:3–47.

[20] Scheffler DR, Zukas JA. Practical aspects of numerical simulation of dynamic events: material interfaces. Int J Impact Eng 2000;24(8):821–42.